AIAA-94-1428-CP

COMPUTATIONS OF VORTEX-BREAKDOWN INDUCED TAIL BUFFET UNDERGOING BENDING AND TORSIONAL VIBRATIONS

Osama A. Kandil*, Steven J. Massey† and Hamdy A. Kandil‡
Aerospace Engineering Department
Old Dominion University, Norfolk, VA 23529–0247

ABSTRACT

A delta wing-vertical tail configuration is used to computationally simulate the vertical-tail buffet problem. The configuration consists of a sharp-edged, delta wing of aspect ratio one and a rectangular, vertical plate of aspect ratio one, which is placed in the plane of geometric symmetry behind the wing with the tail lower edge clamped. The configuration angle of attack is 35°, which results in the breakdown of the primary-vortex cores of the delta wing. The present multidisciplinary problem is solved successively at each time step using three sets of equations for the fluid flow, aeroelastic deflections and grid displacements. The flowfield is obtained using the unsteady, compressible, full Navier-Stokes equations; and the aeroelastic deflections of the tail are obtained using the coupled aeroelastic equations for bending and torsional vibrations. The grid displacements are obtained using interpolation equations. The results show substantial effects of torsional deflections of the tail for the coupled bending-torsion response case in comparison with the bending response case. The results also show that the deflections and loads of the coupled bending-torsion response case are substantially lower than those of the uncoupled bending-torsion response case.

INTRODUCTION

Very recently, substantial research interest has developed in the multidisciplinary engineering problems, particularly in the aeronautical applications. The design of modern fighter aircraft has been focused on high angle of attack maneuverability at high loading conditions, renewing the interest in the tail buffet problem. For these fighters, the ability to fly and maneuver at high angles of attack is of prime importance. This capability is achieved, for example in the F/A-18 fighter, through the combination of the leading-edge extension (LEX) and a delta wing and the use of vertical tails. The LEX maintains lift at high angles of attack by generating a pair of vortices that trail aft over the top of the aircraft. The vortex entrains air over the vertical tails to maintain stability of the aircraft. This combination of LEX and vertical tails leads to the aircraft excellent high angle of attack performance. However, at some flight conditions, the vortices emananting from the highly-swept LEX of the delta wing breakdown before reaching the vertical tails which get bathed in a wake of highly-turbulent, swirling flow. The vortex-breakdown flow produces severe buffet on the vertical tails and has led to their premature fatigue failure.

Experimental investigation of the vertical tail buffet of the F/A-18 models have recently been conducted by several investigators such as Sellers et al.[1], Erickson et al.[2], Wentz[3] and Lee and Brown[4]. These experiments showed that the vortex produced by the LEX of the wing breaks down ahead of the vertical tails at angles of attack of 25° and higher and the breakdown flow produced unsteady loads on the vertical tails. Rao, Puram and Shah[5] proposed two aerodynamic concepts for alleviating high-alpha tail buffet characteristics of the twin tail fighter configurations. Cole, Moss and Doggett[6] tested a rigid, 1/6 size, full-span model of an F-18 airplane that was fitted with flexible vertical tails of two different stiffness. Vertical-tail buffet response results were obtained over the range of angles of attack from −10° to +40°, and over the range of Mach numbers from 0.3 to 0.95. Their results indicated that the buffet response occurs in the first bending mode, increases with increasing dynamic pressure and is larger at M = 0.3 than that at a higher Mach number.

An extensive experimental investigation has been conducted to study vortex-fin interaction on a twin-fin configuration by Washburn, Jenkins and Ferman[6]. The configuration consisted of a 76° sharp-edged delta wing with vertical tails mounted behind the wing. The vertical tails were placed at nine locations behind the wing. The experimental data showed that the aerodynamic loads are more sensitive to the chordwise tail location than its spanwise location. As the tails were moved toward the vortex core, the buffeting response and excitation were reduced. Although the tail location did not affect the vortex core trajectories, it affected the location of vortex-core breakdown. Moreover, the investigation showed that the presence of a flexible tail can affect the unsteady pressures on the rigid tail on the opposite side of the model.

Kandil, Kandil and Massey[8] presented the first successful computational simulation of the vertical tail buffet using a delta wing-vertical tail configuration. A 76° sharp-edged delta wing has been used along with a single rectangular vertical tail which was placed aft the wing along the plane of geometric symmetry. The flow conditions and wing angle of attack have been selected to produce an unsteady vortex-breakdown flow. The solution of this multidisciplinary problem was obtained using three sets of equations (Navier-Stokes, aeroelastic and grid-displacement equations) which were sequentially inte-

* Professor, Eminent Scholar and Department Chairman; Associate Fellow AIAA.
† Graduate Research Assistant, Member AIAA
‡ Research Assistant Professor, Member AIAA.
Copyright © 1994 by Osama A. Kandil. Published by The American Institute of Aeronautics and Astronautics, Inc. with Permission.

grated with time-accurate stepping to obtain the flowfield, aerodynamic loads, bending deflections and grid displacements. Two tail aspect ratios with two chordal locations were used. Unsteady vortex breakdown of leading-edge vortex cores was captured, and unsteady pressure forces were obtained on the tail. Tail shapes and locations were found to affect the vortex breakdown locations and aerodynamic loads on the wing and tail. The tail oscillated in the first bending-mode shape. These computational results are in full qualitative agreement with the experimental data of Washburn, Jenkins and Ferman[7]. An alternative simple model for simulation of the buffet problem was used by Kandil and Flanagan[8] and Flanagan[9]. In this model, a configured circular duct was used to produce vortex-breakdown flow through the interaction of a supersonic swirling flow and a shock at the inlet of the duct. Downstream of the vortex-breakdown flow a cantilevered plate was placed. The problem was solved for the quasi-axisymmetric case. Currently, this model is used to simulate the three-dimensional flow buffet problem.

In the present paper, the delta wing-vertical tail configuration is used to study the buffet problem, where the vertical tail is allowed to oscillate in both bending and torsional modes. In Ref. 8, by the present authors, only the bending-mode oscillation was considered. It was also noticed in Ref. 8 that torsional aerodynamic loads appeared on the tail but their aeroelastic effects were neglected. In the present paper, we address the cases of coupled and uncoupled bending-torsional responses of the tail.

FORMULATION

The formulation of the problem consists of three sets of governing equations along with certain initial and boundary conditions. The first set is the laminar, unsteady, compressible, full Navier-Stokes equations. The second set consists of the aeroelastic equations which include bending and torsional modes. The third set consists of equations for calculating the grid displacements due to the tail deflections. The literature shows various methods to move the grid. The simplest method uses simple interpolation functions such that the grid points adjacent to the aeroelastic surface move with the surface while the grid points at the computational-region boundary do not move[11,12]. In the more advanced methods for moving the grid, the grid is simulated as a static[13-15] or dynamic truss. The unsteady, linearized, Navier-displacement equations have also been used successfully by Kandil et al. to move the grid dynamically[16,17]. In the present paper, we use simple grid interpolation to move the grid. Next, the governing equations for each set are given:

Fluid-Flow Equations:

The conservative form of the dimensionless, unsteady, compressible, full NS equations in terms of time-dependent, body-conformed coordinates ξ^1, ξ^2 and ξ^3 is given by

$$\frac{\partial \bar{Q}}{\partial t} + \frac{\partial \bar{E}_m}{\partial \xi^m} - \frac{\partial (\bar{E}_v)_s}{\partial \xi^s} = 0; m = 1-3, s = 1-3 \quad (1)$$

where

$$\xi^m = \xi^m(x_1, x_2, x_3, t) \quad (2)$$

$$\bar{Q} = \frac{\hat{q}}{J} = \frac{1}{J}[\rho, \rho u_1, \rho u_2, \rho u_3, \rho e]^t, \quad (3)$$

$\bar{E}_m$ and $(\bar{E}_v)_s$ are the inviscid flux and viscous and heat-conduction flux in ξ^s direction, respectively. Details of these fluxes are given in Ref. 8 by the authors.

Aeroelastic Deflections:

In the present paper, we consider the dimensionless, linearized governing equations for the coupled bending and torsional vibrations of a vertical tail that is treated as a cantilevered beam. The tail bending and torsional deflections occur about an elastic axis that is displaced from the inertial axis. These equations for the bending deflection, w, and the twist angle, θ, are given by

$$\frac{\partial^2}{\partial z^2}\left[EI(z)\frac{\partial^2 w}{\partial z^2}(z,t)\right] + m(z)\frac{\partial^2 w}{\partial t^2}(z,t) + m(z)x_\theta(z)\frac{\partial^2 \theta}{\partial t^2}(z,t) = N(z,t) \quad (4)$$

$$\frac{\partial}{\partial z}\left[GJ(z)\frac{\partial \theta}{\partial z}\right] - m(z)x_\theta\frac{\partial^2 w}{\partial t^2}(z,t) - I_\theta(z)\frac{\partial^2 \theta}{\partial t^2}(z,t) = -M_t(z,t) \quad (5)$$

where z is the vertical distance from the fixed support along the tail length, l_t, EI and GJ the bending and torsional stiffness of the tail section, m the mass per unit length, I_θ the mass-moment of inertia per unit length about the elastic axis, x_θ the distance between the elastic axis and inertia axis, N the normal force per unit length and M_t the twisting moment per unit length. The characteristic parameters for the dimensionless equations, Eqs. (4) and (5), are c^*, a^*_∞, ρ^*_∞ and c^*/a^*_∞ for the length, speed, density and time; where c^* is the delta-wing root-chord length, a^*_∞ the freestream speed of sound and ρ^*_∞ the freestream air density. The geometrical and natural boundary conditions on w and θ are given by

$$\omega(0,t) = \frac{\partial w}{\partial z}(0,t) = \frac{\partial^2 w}{\partial z^2}(l_t,t) = \frac{\partial}{\partial_z}\left[EI(l_t)\frac{\partial^2 w}{\partial z^2}(l_t,t)\right] = 0 \quad (6)$$

$$\theta(0,t) = \frac{\partial \theta}{\partial z}(l_t,t) = 0 \quad (7)$$

The solution of Eqs. (4) and (5) are given by

$$w(z,t) = \sum_{i=1}^{\hat{I}} \phi_i(z) q_i(t) \quad (8)$$

$$\theta(z,t) = \sum_{j=\hat{I}+1}^{M} \phi_j(z) q_j(t) \tag{9}$$

where ϕ_i and ϕ_j are comparison functions satisfying the free-vibration modes of bending and torsion, respectively, and q_i and q_j are generalized coordinates for bending and torsion, respectively. In this paper, the number of bending modes, $\hat{I}$, is six and the number of torsion modes, $M - \hat{I}$, is also six. Substituting Eqs. (8) and (9) into Eqs. (4) and (5) and using the Galerkin method along with integration by parts and the boundary conditions, Eqs. (6) and (7), we get the following equations for the generalized coordinates q_i and q_j:

$$\sum_{i=1}^{\hat{I}} q_i \int_o^{l_t} EI \frac{d^2\phi_r}{dz^2}\frac{d^2\phi_i}{dz^2} dz + \sum_{i=1}^{\hat{I}} \ddot{q}_i \int_o^{l_t} m\phi_r\phi_i dz + \sum_{j=\hat{I}+1}^{M} \ddot{q}_j \int_o^{l_t} m x_\theta \phi_r \phi_j dz - \int_o^{l_t} \phi_r N dz = 0 \tag{10}$$

$$\sum_{j=\hat{I}+1}^{M} q_i \int_o^{l_t} GJ \frac{d\phi_s}{dz}\frac{d\phi_j}{dz} dz + \sum_{i=1}^{\hat{I}} \ddot{q}_i \int_o^{l_t} m x_\theta \phi_s \phi_i dz + \sum_{j=\hat{I}+1}^{M} \ddot{q}_j \int_o^{l_t} I_\theta \phi_s \phi_j dz - \int_o^{l_t} M_t \theta_s dz = 0 \tag{11}$$

Equations (10) and (11) may be written in the matrix form

$$\begin{bmatrix} M_{11} & M_{12} \\ M_{21} & M_{22} \end{bmatrix} \begin{Bmatrix} \ddot{q}_i \\ \ddot{q}_j \end{Bmatrix} + \begin{bmatrix} K_{11} & 0 \\ 0 & K_{22} \end{bmatrix} \begin{Bmatrix} q_i \\ q_j \end{Bmatrix} = \begin{Bmatrix} \hat{N}_1 \\ \hat{N}_2 \end{Bmatrix} ; \begin{matrix} i = 1, 2, \ldots, \hat{I} \\ j = \hat{I}+1, \ldots, M \end{matrix} \tag{12}$$

where

$$M_{11} = \int_o^{l_t} m\phi_r\phi_i dz$$

$$M_{12} = M_{21} = \int_o^{l_t} m x_\theta \phi_r \phi_j dz$$

$$M_{22} = \int_o^{l_t} I_\theta \phi_s \phi_j dz \tag{13}$$

$$K_{11} = \int_o^{l_t} EI \frac{d^2\phi_r}{dz^2}\frac{d^2\phi_i}{dz^2} dz$$

$$K_{22} = \int_o^{l_t} GJ \frac{d\phi_s}{dz}\frac{d\phi_j}{dz} dz \tag{14}$$

$$\hat{N}_1 = \int_o^{l_t} \phi_r N dz$$

$$\hat{N}_2 = \int_o^{l_t} M_t \phi_s dz \tag{15}$$

Similar aeroelastic equations were developed for subsonic analysis of wing flutter by Strganac[18], and Strganac, Mook and Mitchum[19]. The solution of Eq. (12), for q_i; $i = 1, 2, \ldots, \hat{I}$, and q_j; $j = \hat{I}+1, \ldots, M$, is obtained using the Runge-Kutta scheme. Next, w and θ are obtained from Eqs. (8) and (9).

Grid Displacement Equations:

Once w and θ are obtained at the $n+1$ time step, the new grid coordinates are obtained using simple interpolation equations. In these equations, the tail bending displacement, $w_{i,j,k}^{n+1}$, and the tail displacement through the torsion angle, $\theta_{i,j,k}^{n+1}$, are interpolated through a cosine function. These equations for the x and y coordinates to the right side of the tail and ahead of its elastic axis are given by

$$y_{i,j,k}^{n+1} = y_{i,j,k}^{n} + \left[w_{i,j,k}^{n+1} + \left(X - x_{i,j,k}^{n}\right)\sin\theta_{i,j,k}^{n+1}\right]\cos\left(\frac{y_{i,j,k}^{n}}{Y}\frac{\pi}{2}\right) \tag{16}$$

$$x_{i,j,k}^{n+1} = x_{i,j,k}^{n} + \left(X - x_{i,j,k}^{n}\right)\left(1 - \cos\theta_{i,j,k}^{n+1}\right)\cos\left(\frac{x_{i,j,k}^{n}}{X}\frac{\pi}{2}\right) \tag{17}$$

where $x_{i,j,k}^{n+1}$ and $y_{i,j,k}^{n+1}$ are the x and y coordinates of a grid point at the $n+1$ time step, Y is the maximum y coordinate from the tail-surface grid point to the corresponding point at the right boundary of the computational domain and X is the maximum x coordinate from the tail elastic axis to the forward boundary of the computational domain. These equations result in displacing a grid point on the tail by the total deflection due to bending and torsion and keeping a grid point at the boundary fixed. Similar equations are used for the other parts of the computational domain.

Boundary and Initial Conditions:

Boundary conditions consist of conditions for the fluid flow and conditions for the aeroelastic bending and torsional deflections of the tail. For the fluid flow, the Riemann-invariant boundary conditions are enforced at the inflow and outflow boundaries of the computational domain. At the plane of geometric symmetry, a periodic boundary condition is specified with the exception of grid points on the tail. On the wing surfaces, the no-slip and no-penetration conditions are enforced and $\frac{\partial p}{\partial n} = 0$. On the tail surfaces, the no-slip and no-penetration conditions for the relative velocity components are enforced (points on the tail surface are moving). The normal pressure gradient is no longer equal to zero since points on the tail surface are accelerating. This condition becomes $\frac{\partial p}{\partial n} = -\rho \bar{a}_t \cdot \hat{n}$, where $\bar{a}_t$ is the acceleration of a point on the tail, which is given by:

$$\bar{a}_t = -r\left[\frac{\partial^2\theta}{\partial t^2}\sin\theta + \left(\frac{\partial\theta}{\partial t}\right)^2\cos\theta\right]\hat{i} + \left\{\frac{\partial^2 w}{\partial t^2} + r\left[\frac{\partial^2\theta}{\partial t^2}\cos\theta - \left(\frac{\partial\theta}{\partial t}\right)^2\sin\theta\right]\right\}\hat{j} \tag{18}$$

where r is the point distance from the tail elastic axis. For the boundary conditions on the aeroelastic deflections of the tail, they are given by Eqs. (6) and (7).

Initial conditions consist of conditions for the fluid flow and conditions for the aeroelastic deflections of the

tail. For the fluid flow, the initial conditions correspond to the freestream conditions with $u_1 = u_2 = u_3 = 0$ on the wing and tail. For the aeroelastic deflections of the tail, the initial conditions for any point on the tail is that the displacement and velocity are zeros, $w(z,0) = \frac{\partial w}{\partial t}(z,0) = 0$, $\theta(z,0) = \frac{\partial \theta}{\partial t}(z,0) = 0$.

METHOD OF SOLUTION

The first step is to solve for the fluid-flow problem using the vortex-breakdown conditions and keeping the tail as a rigid beam. Equations (1)-(3) are solved time-accurately using the implicit, upwind, flux-vector splitting finite-volume scheme. The grid speed $\frac{\partial \xi^m}{\partial t}$ is set equal to zero in this step. This step provides the flowfield solution along with the pressure difference across the tail. The pressure difference is used to generate the normal force and twisting moment per unit length of the tail. Next, Eqs. (8), (9) and (12) are used to obtain the tail deflections, $w_{i,j,k}$ and $\theta_{i,j,k}$. Equations (16) and (17) are used to compute the grid coordinates. The metric coefficients of the coordinate Jacobian matrix are updated as well as the grid speed, $\frac{\partial \xi^m}{\partial t}$. Next, the computational cycle is repeated every time step. It should be noted that the time step for the fluid-flow problem, Δt_f, does not have to be the same as the time step for the aeroelastic deflection, Δt_d. Moreover, the maximum tail deflections w and θ for each Δt_d are very small. Hence, one does not need to compute w and θ for each time step Δt_f. For example, if $\Delta t_d = 10\ \Delta t_f$, the computation of the aeroelastic deflections and grid coordinates can be performed every $10\ \Delta t_f$.

Equation (12) can also be used to compute w and θ for the uncoupled case of bending and torsional vibrations by setting $x_\theta = 0$. Moreover, Eq. (12) can be used to compute w for the bending vibrations only by setting $x_\theta = 0$ and the resulting $\theta = 0$ at each time step. For this case, Eqs. (16) and (17) compute the coordinates $y^{n+1}_{i,j,k}$ while keeping the x coordinate stationary.

COMPUTATIONAL APPLICATIONS

Delta Wing-Vertical Tail Configuration:

The delta wing-vertical tail configuration consists of a sharp-edged, delta wing of aspect ratio 1 and a rectangular, vertical tail of aspect ratio 1, which is placed in the plane of geometric symmetry. The vertical-tail leading edge is located at the wing trailing edge. The lower edge of the tail is along the wing axis and the tail is clamped at that edge. The wing angle of attack is 35° and the freestream Mach number and Reynolds number are 0.4 and 10,000, respectively. An O-H grid of $125 \times 85 \times 84$ grid points in the wrap-around, normal and axial directions, respectively, is used for the solution of the fluid-flow part of the problem.

Initial Conditions (Solution of Fluid-Flow Problem):

The laminar, unsteady, compressible, full Navier-Stokes equations have been integrated time accurately using the implicit, upwind, flux-vector splitting, finite-volume scheme with $\Delta t = 0.003$. During this step, the tail is kept rigid. The results of this step are used as initial conditions for the cases of bending response, coupled bending-torsion response and uncoupled bending-torsion response of the tail.

Figure 1 shows a top view and a three-dimensional view at it = 14,600 for the wing-rigid tail configuration along with the critical points of vortex breakdown and the stagnation pressure on the wing and tail. This figure shows that the vortex breakdown is asymmetric. Figure 2 shows the same type of views for the case of a rigid tail at it = 16,600. These results show different locations of the critical points of vortex-breakdown, different stagnation-pressure distributions on the wing and tail. This conclusively shows that the vortex-breakdown flow and the aerodynamic loads on the wing and tail are time dependent. Figure 3 shows the spanwise, surface pressure coefficient (C_p) on the wing at different chord stations at it = 14,600 and 16,600 for the rigid tail. In Fig. 3.a at $x = 0.448$, the C_p curve is asymmetric with the left side having less suction than the pressure on the right side. This indicates that the left-side vortex core (looking in the upstream direction — Fig. 1) is experiencing vortex breakdown and enlarging at a location ahead of that of the right-side vortex core. It is also noticed that the C_p-asymmetry exists in all cross-flow planes downstream of $x = 0.25$. At $x = 0.95$, a rapid decrease in the suction pressure is noticed and Fig. 1 shows that the breakdown is of the spiral type thereafter. With the exception of the C_p-curve at $x = 0.25$, Fig. 3b shows different C_p asymmetry and levels than those of Fig. 3.a. Figure 2 shows different locations of the vortex-cores breakdown than those of Fig. 1. Again, these results show that the vortex-core breakdown and aerodynamic loads for the rigid tail are time dependent.

Bending, Coupled Bending-Torsion and Uncoupled Bending-Torsion Tail Responses:

With the initial-flow conditions obtained at it = 14,600, the problem is solved for three aeroelastic response cases. These are the bending, coupled bending-torsion, uncoupled bending-torsion responses of the tail. The tail is treated as a rectangular beam with thickness $d = 0.005$, width $b = 0.5$ and height $l_t = 0.5$. The tail material dimensionless modulii of elasticity and rigidity, E and G, are 1.8×10^5 and 0.692×10^5, respectively. For the coupled bending-torsion case, the tail mass is assumed to vary in the x direction resulting into the distance between the elastic axis and inertia axis of $x_\theta = 0.05$ (inertia axis is downstream of the elastic axis). For the uncoupled bending-torsion case no mass variation is assumed, hence, $x_\theta = 0$. The mass per unit length, m, is taken

as 0.0653 and the mass-moment of inertia per unit length around the elastic axis, I_θ, is 0.00153.

Figures 4 and 5 show a top view and a three-dimensional view of the critical points of vortex breakdown and the stagnation pressures on the wing and tail for the bending tail response and the bending-torsion response, respectively.

The results show that the locations of vortex breakdown and stagnation-pressure distributions on the wing and tail for the bending response are different from those of the bending-torsion response. They are also different from the case of rigid tail at the same time step of it = 16,600 (Fig. 2). These results conclusively show the upstream effect of the tail response type on the vortex breakdown location and the pressure distribution on the wing and the tail.

For the rigid tail, Fig. 6 shows the variation of the normal-force per unit length along the tail height at different time steps, covering the range it = 14,601–17,000 (curves A, $B, \ldots J$ at 14,601; 14,900;...; 17,000). The figure also shows the normal-force variation at the tail tip vz time.

For the bending tail response, Fig. 7 shows the history of bending deflection and normal force per unit length vz tail height at different time steps covering the range it = 14,601–17,600. The bending vibration is clearly occurring in the first bending mode shape. The bending deflections and normal force per unit length vz time for the tail tip and midpoint are also given in Fig. 7. Studying these results, the following conclusions are reached: the normal-force and bending-deflection curves show large amplitudes in the first 1,500 time steps. Thereafter, they are suppressed by the aerodynamic damping force. The frequencies of the normal force are much higher than the frequencies of the bending deflection. No periodic response has been found within the computational time period of 3000 time steps.

Figures 8 and 9 show the results for the coupled bending-torsion response of the tail. Figure 8 shows that the torsional deflection angles, hence, the torsional deflections are higher than the bending deflections. Both bending and torsional deflections for the coupled case are noticed to be one order of magnitude higher than the bending deflection case of Fig. 7. For the coupled case, the frequencies of the normal-force and twisting-moment per unit length are higher than the frequencies of the bending and torsion deflections. The bending and torsion loads and deflections are suppressed by the aerodynamic damping force up to the time step 5,800. No periodic response has been found within the computational time period of 7000 time steps.

Figures 10 and 11 show the results for the uncoupled bending-torsion response of the tail ($x_\theta = 0$). The bending and torsion deflections are almost twice as large as the bending and torsion deflections of the coupled case (Figs. 8 and 9). Again, both the deflections and loads are suppressed by the aerodynamic damping force. It is also noticed that the frequencies of the loads for this case are not as high as those for the coupled case.

Figures 12 and 13 show the history of the tail total deflection vz the tail height for the coupled and uncoupled cases, respectively. It is observed that the maximum deflections of the uncoupled case are more than twice those of the coupled case. In the same figures, a three-dimensional view of the deformed tail is given showing its shape at it = 21,600 for the coupled case and it = 21,000 for the uncoupled case. Figure 14 shows the cross-flow instantaneous streamlines at different chord stations passing through the tail at it = 21,000 for the coupled case. It is observed that the vortex-breakdown flow moves closer to and upward of the tail as the flow moves downstream. In Fig. 15, the spanwise, surface-pressure coefficient at different chord stations on the wing are shown for the coupled case at it = 16,600. This is the same time step for the rigid wing of Fig. 3.b. It is noticed that the suction pressure at x = 0.25 for the coupled case is smaller than that of the rigid tail. At x = 0.9891, the suction pressure for the coupled case is larger than that of the rigid tail. This comparison conclusively shows the upstream effect of the tail deflections on the wing aerodynamic loads.

CONCLUDING REMARKS

The buffet problem of a vertical tail due to the interaction of vortex-breakdown flow with the tail has been simulated computationally and efficiently using a delta wing-vertical tail configuration. The wing aspect ratio and flow conditions have been carefully selected in order to produce unsteady vortex-breakdown flow. The solution has demonstrated the development of the tail buffet due to the unsteady loads produced by the vortex-breakdown flow. The problem is a multidisciplinary problem which requires three sets of equations to obtain its solution.

In the present paper, we considered three tail responses; namely, bending only, coupled bending and torsion and uncoupled bending and torsion. It has been shown that the total deflections of the coupled bending-torsion case are one order of magnitude higher than those of the bending case. Moreover, the frequencies of deflections and loads of the coupled case are higher than those of the bending case. The total deflections of the uncoupled bending-torsion case were more than twice those of the coupled case. This is due to the aeroelastic coupling between the bending and torsion response. A careful study has been performed to show the upstream effect of the tail vibrations on the wing aerodynamic loads. It is conclusively shown that the tail vibrations change the vortex-breakdown locations and the unsteady aerodynamic loads on the wing and tail. These conclusions are in perfect agreement with the experimental data of Ref. 7. Work is underway to upgrade the tail model from beam equations to real tail equations using of finite-element

structural-dynamics computer codes and actively control the buffet response.

ACKNOWLEDGEMENT

This research work is supported under Grant No. NAG-1-648 by the NASA Langley Research Center and the Air Force Office for Scientific Research, Bolling AFB. The authors would like to recognize the computational resources provided by the NAS facilities at Ames Research Center and the NASA Langley Research Center.

REFERENCES

1. Sellers, W. L. III, Meyers, J. F. and Hepner, T. E., "LDV Survey Over a Flighter Model at Moderate to High Angle of Attack," SAE Paper 88–1448, 1988.
2. Erickson, G. E., Hall, R. M., Banks, D. W., Del Frate, J. H., Shreiner, J. A., Hanley, R. J., and Pulley, C. T., "Experimental Investigation of the F/A-18 Vortex Flows at Subsonic Through Transonic Speeds," Invited Paper, AIAA 89–2222, 1989.
3. Wentz, W. H., "Vortex-Fin Interactions on a Fighter Aircraft," AIAA 87–2474, AIAA Fifth Applied Aerodynamics Conference, Monterey, CA, August 1987.
4. Lee, B. and Brown, D., "Wind Tunnel Studies of F/A-18 Tail Buffet," AIAA 90–1432, 1990.
5. Rao, D. M., Puram, C. K. and Shah, G. H., "Vortex Control for Tail Buffet Alleviation on a Twin-Tail Fighter Configuration," SAE Paper No. 89–2221, 1989.
6. Cole, S. R., Moss, S. W. and Doggett, R. V., Jr., "Some Buffet Response Characteristics of a Twin-Vertical-Tail Configuration," NASA TM-102749, October 1990.
7. Washburn, A. E., Jenkins, L. N. and Ferman, M. A., "Experimental Investigation of Vortex-Fin Interaction," AIAA 93–0050, AIAA 31st ASM, Reno, NV, January 11–14, 1993.
8. Kandil, O. A., Kandil, H. A. and Massey, S. J., "Simulation of Tail Buffet Using Delta Wing-Vertical Tail Configuration," AIAA 93–3688–CP, AIAA Atmospheric Flight Mechanics Conference, Monterey, CA, August 9–11, 1993, pp. 566–577.
9. Kandil, O. A. and Flanagan, M. W., "Vertical Tail Buffet in Vortex Breakdown Flows," 5th International Symposium on Computational Fluid Dynamics, Sendai-Japan, August 31–September 3, 1993.
10. Flanagan, M. W., "Simulation of Vertical Tail Buffet in Internal Vortex Breakdown Flows," M.S Thesis, Aerospace Engineering Department, Old Dominion University, Norfolk, VA, December 1993.
11. Ide, H. and Shankar, V. J., "Unsteady Full Potential Aeroelastic Computations for Flexible Configurations," AIAA 87–1238, June 1987.
12. Schuster, D., Vadyak, J. and Atta, E., "Static Aeroelastic Analysis of Fighter Aircraft Using a Three-Dimensional Navier-Stokes Algorithm," AIAA 90–0435, January 1990.
13. Kennon, S. R., "Supersonic Inlet Calculations Using an Upwind Finite-Volume Method on Adaptive Unstructured Grids," AIAA-89-0113, January 1989.
14. Morgan, K., Peraive, J., Thareja, R. R. and Stewart, J. R., "An Adaptive Finite Element Scheme for the Euler and Navier-Stokes Equations," AIAA-87-1172, June 1987.
15. Batina, J., "Unsteady Euler Airfoil Solutions Using Unstructured Dynamic Meshes," AIAA 89-0115, January 1989.
16. Kandil, O. A., Chuang, H. A. and Salman, A. A., "Unsteady Flow Computation of Oscillating Flexible Wings," AIAA-90-0937-CP, April 1990, pp. 1370–1381.
17. Kandil, O. A. and Salman, A. A., "Unsteady Vortex-Dominated Flow Around Wings with Oscillating Leading-Edge Flaps," AIAA 91-0435, January 1991.
18. Strganac, T. W., "A Numerical Model of Unsteady, Subsonic Aeroelastic Behavior," NASA Technical Memorandum 100487, December 1987.
19. Strganac, T. W., Mook, D. T. and Mitchum, M. W., "The Numerical Simulatin of Subsonic Flutter," AIAA 87–1428, June 8–10, 1987.

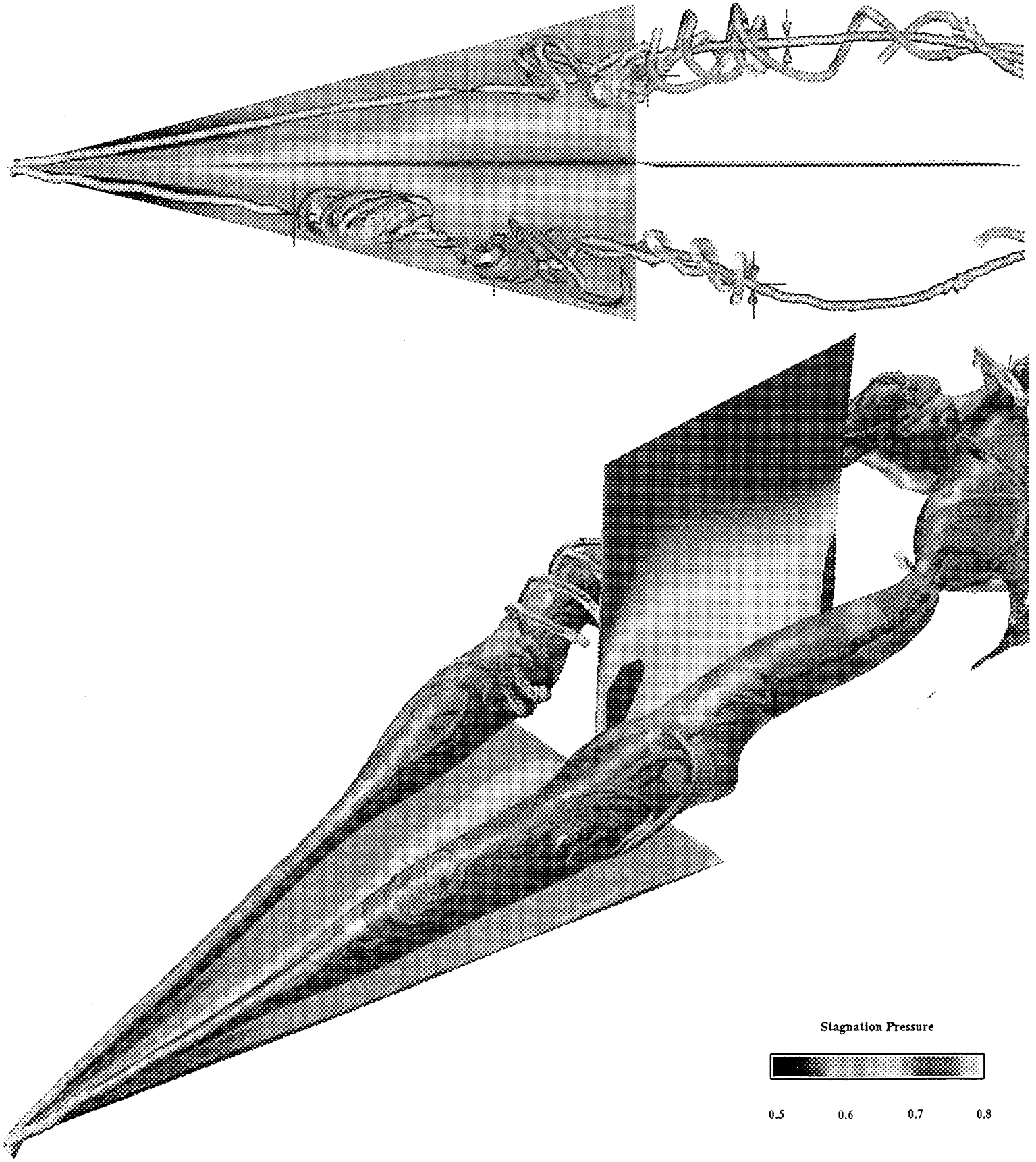

Fig. 1 Top and three-dimensional views showing critical points of vortex breakdown and stagnation pressures on the wing and tail, $M_\infty = 0.4$, $R_e = 10{,}000$, $\alpha = 35°$, $AR_w = 1.0$, $AR_t = 1.0$, it = 14,600 (Rigid tail-Initial conditions).

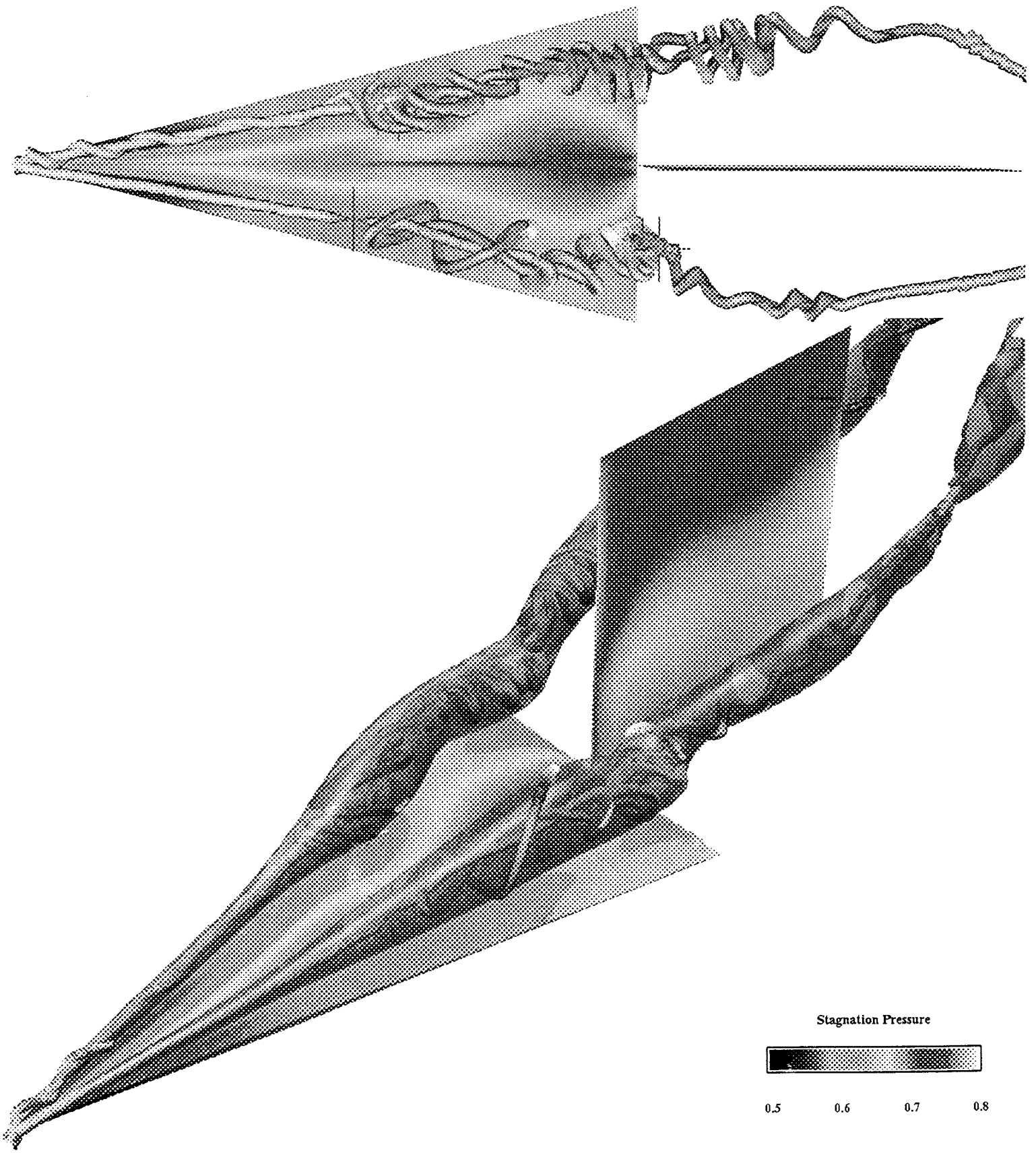

Fig. 2 Top and three-dimensional views showing critical points of vortex breakdown and stagnation pressures on the wing and tail, it = 16,600 (Rigid tail).

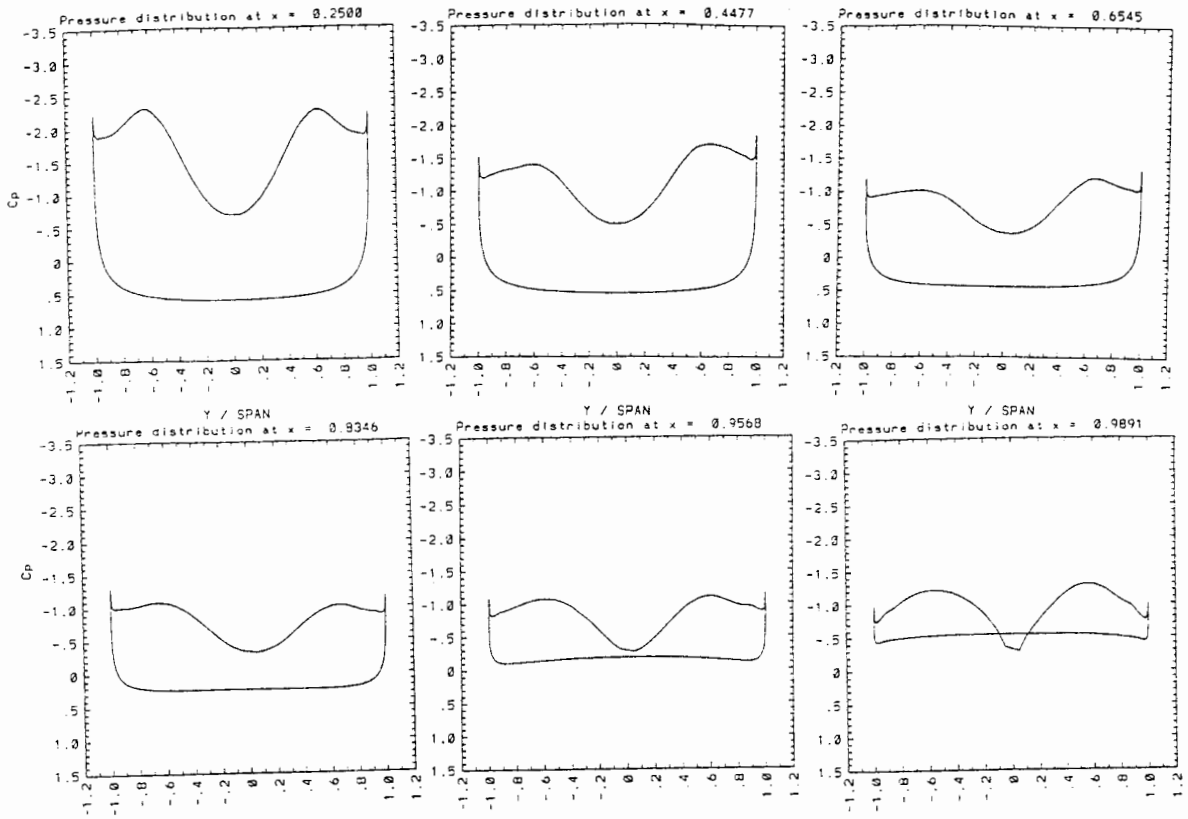

Fig. 3.a Spanwise, surface-pressure coefficient at different chord stations on the wing; it = 14,600 (Rigid tail-Initial conditions).

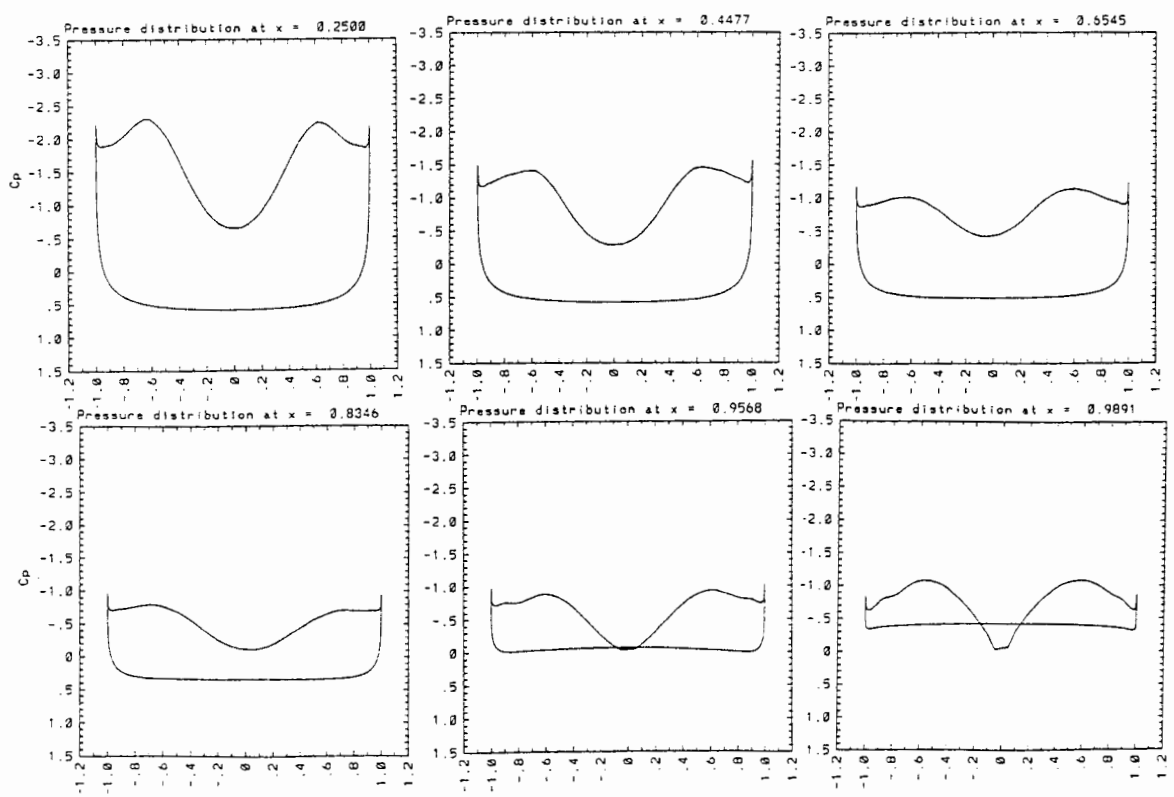

Fig. 3.b Spanwise, surface-pressure coefficient at different chord stations on the wing; it = 16,600 (Rigid tail).

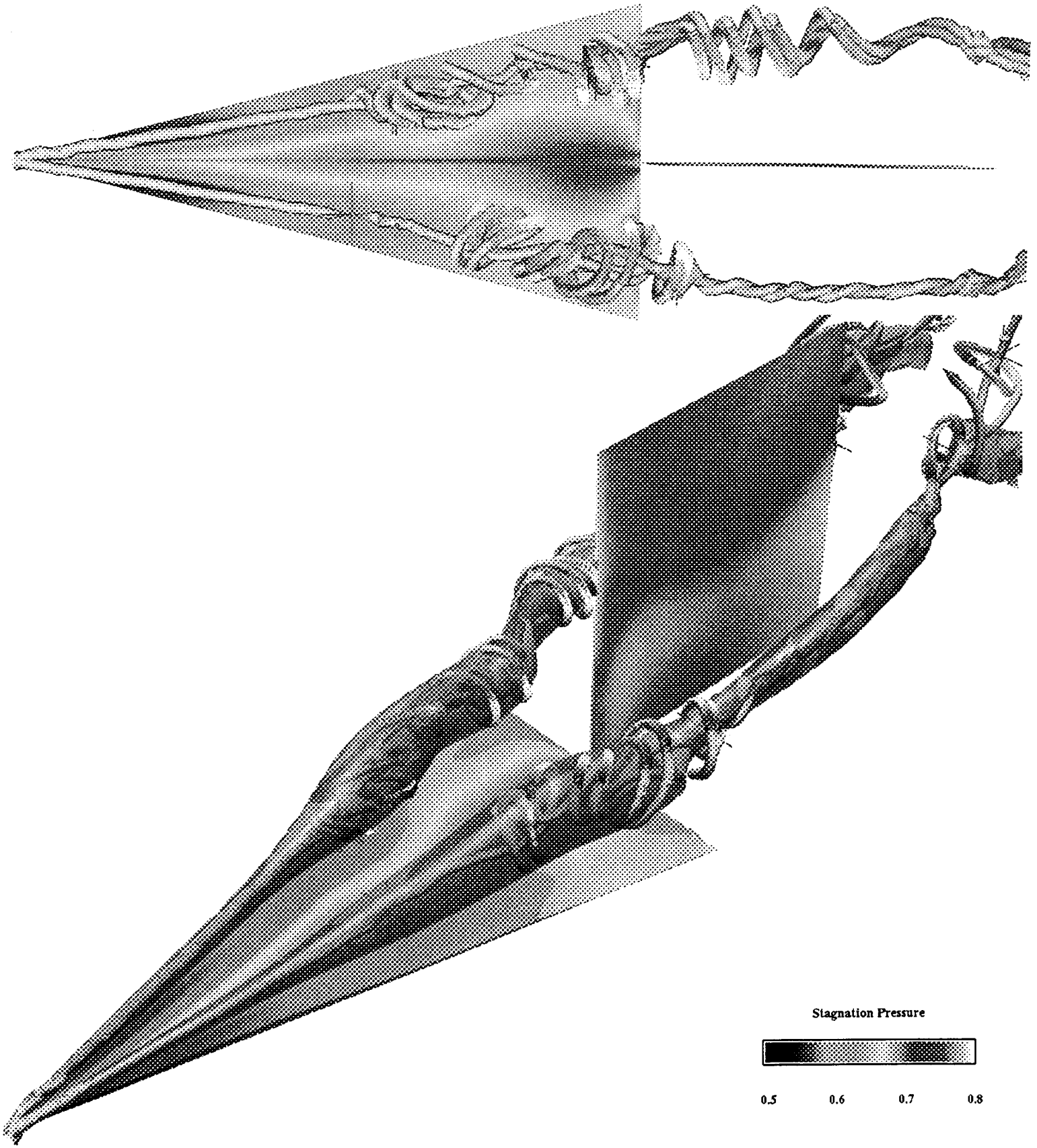

Fig. 4 Top and three-dimensional views showing critical points of vortex breakdown and stagnation pressures on the wing and tail, it = 16,600 (Bending-tail response).

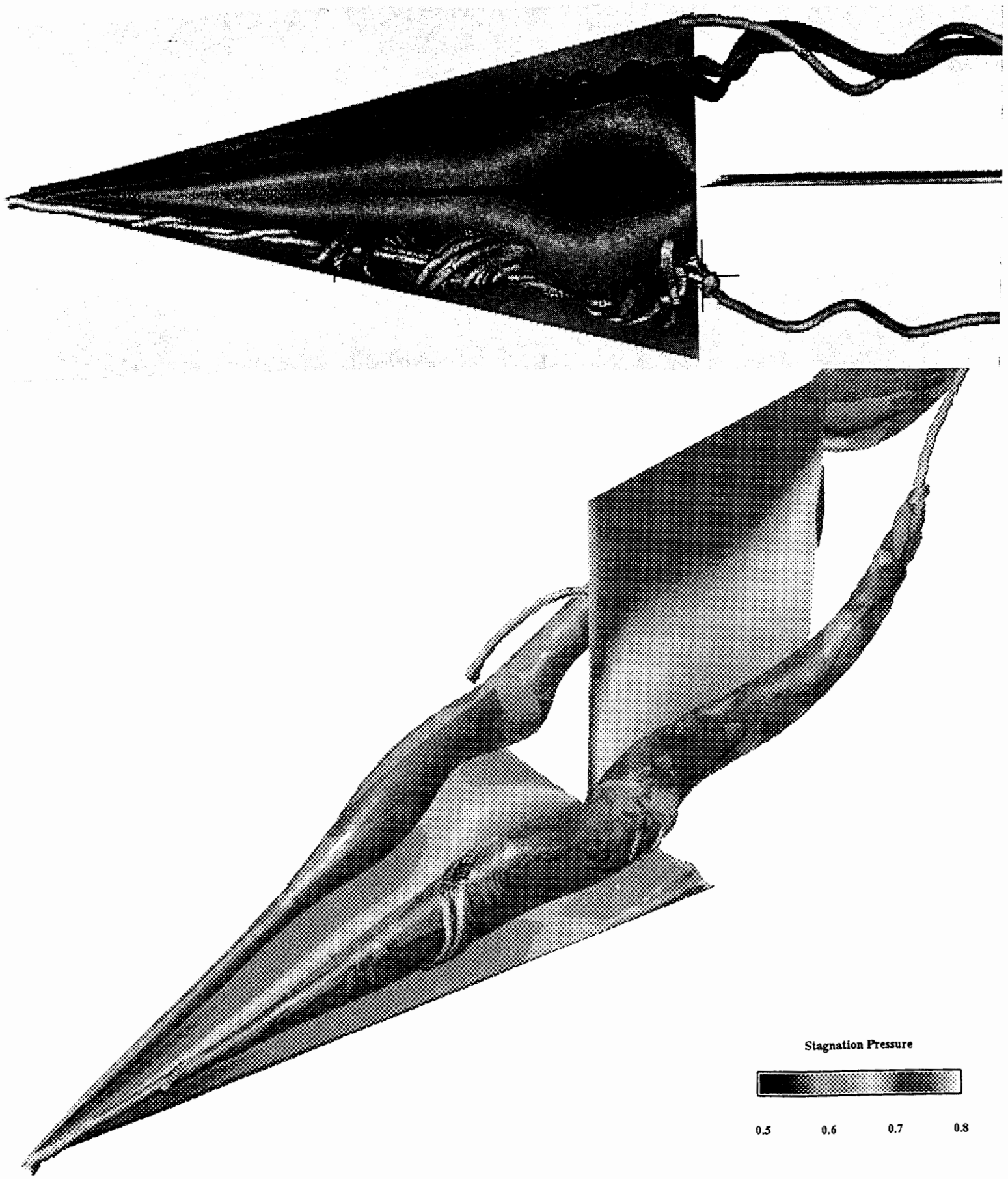

Fig. 5 Top and three-dimensional views showing critical points of vortex breakdown and stagnation pressures on the wing and tail, it = 16,600 (coupled bending and torsional tail response).

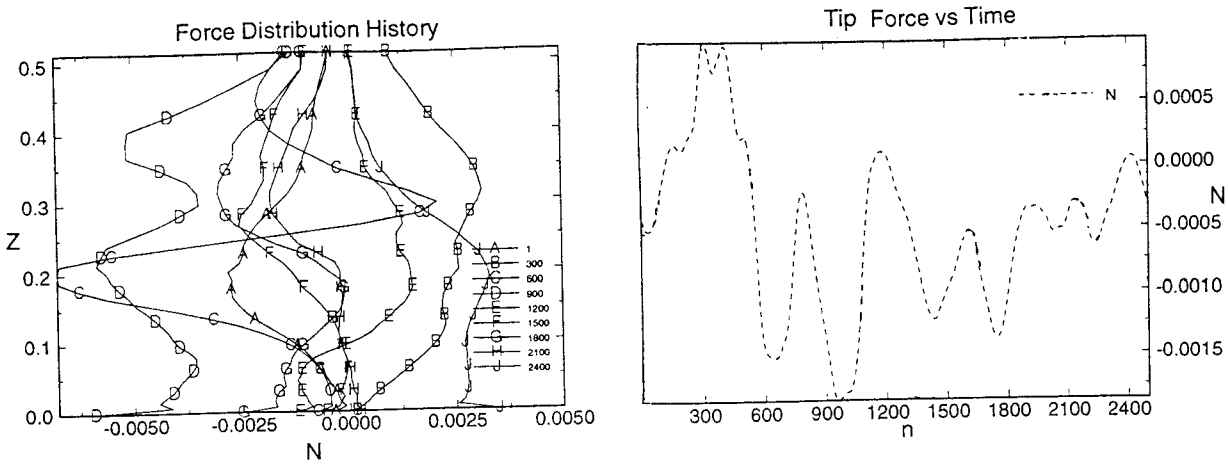

Fig. 6 History of normal force per unit length over the tail and the tip normal force per unit length vz time, it = 14,601–17,000 (Rigid tail).

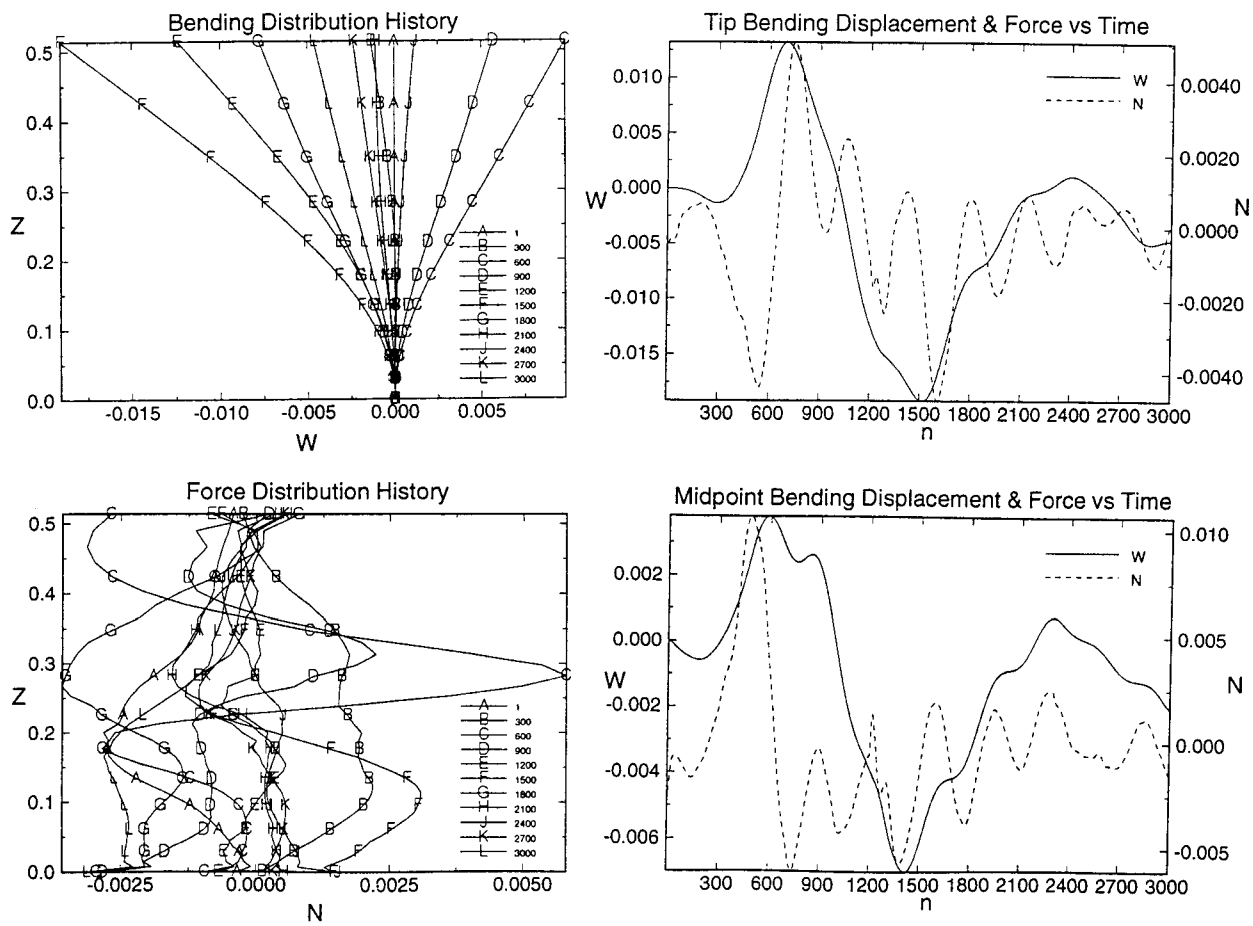

Fig. 7 History of tail deflection and normal force per unit length over the tail and the tip and mid point deflections and normal forces vz time, it = 14,601–17,600 (Bending-tail response).

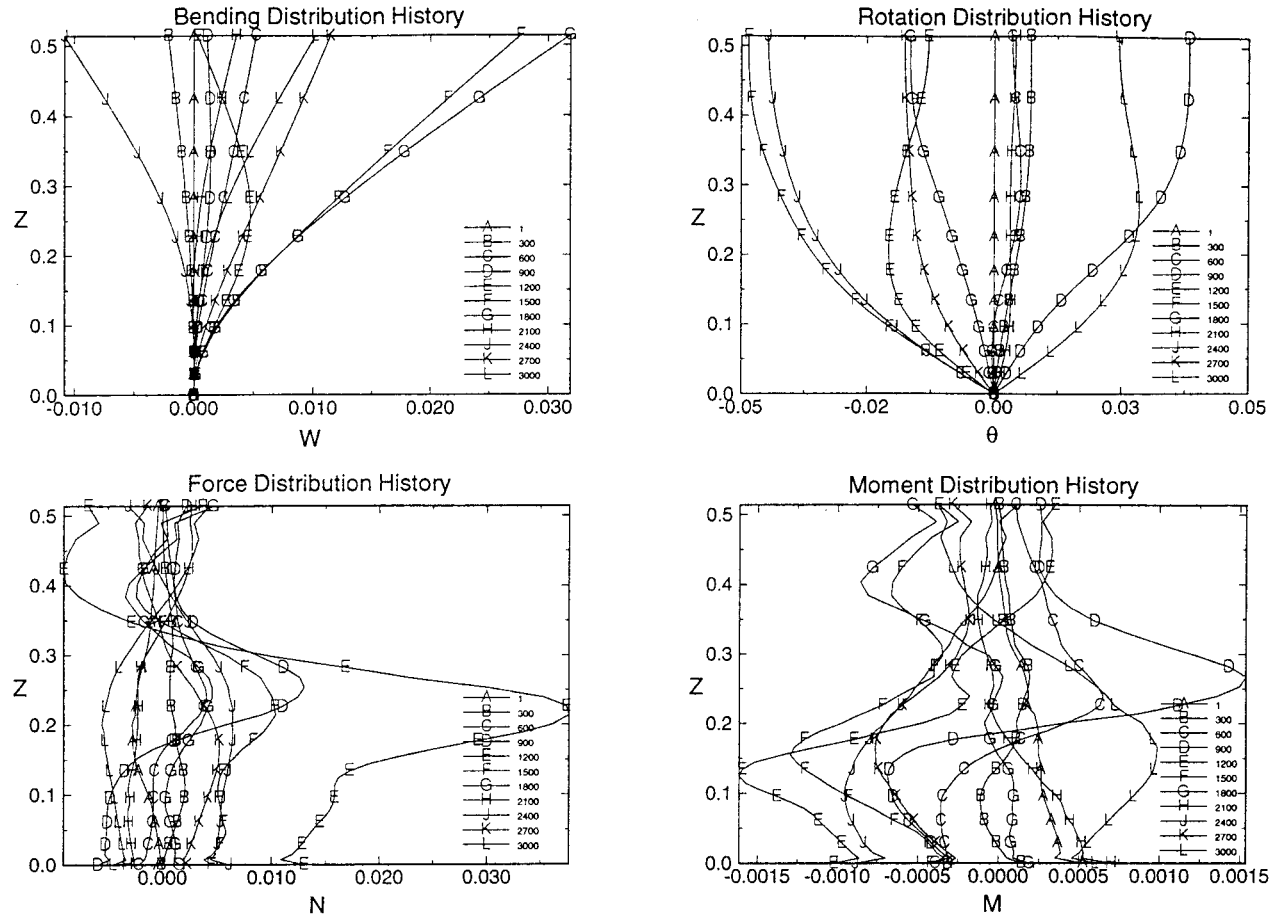

Fig. 8 History of tail deflections, normal-force and twisting-moment per unit length over the tail, it = 14,601–17,600 (coupled bending-torsion tail response).

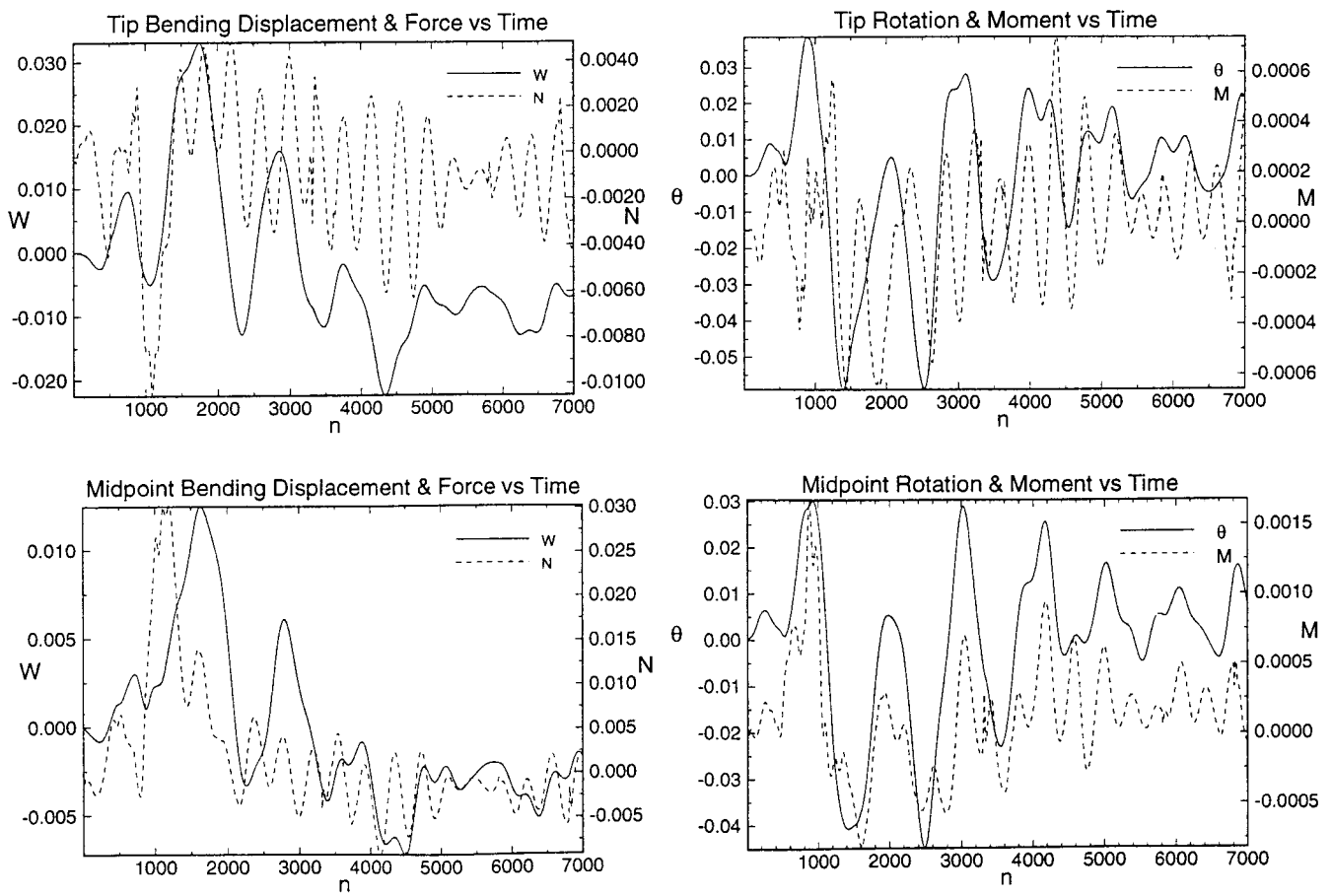

Fig. 9 History of tail deflections, normal-force and twisting-moment per unit length vz time for the tail tip and midpoint, it = 14,601–21,600 (coupled bending-torsion tail response).

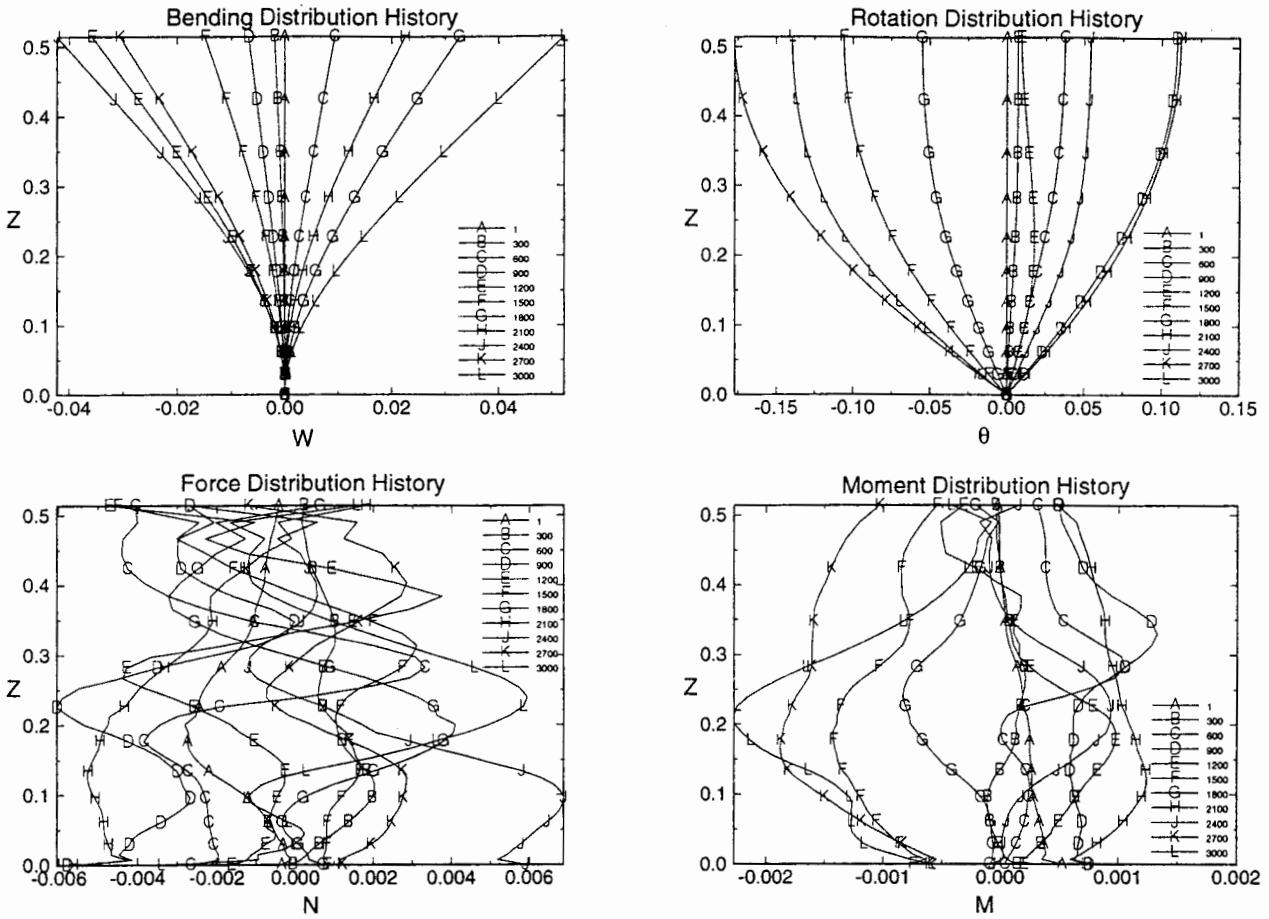

Fig. 10 History of tail total deflections, normal-force and twisting-moment per unit length vz time for the tail tip and midpoint, it = 14,601–17,600 (uncoupled bending-torsion tail response).

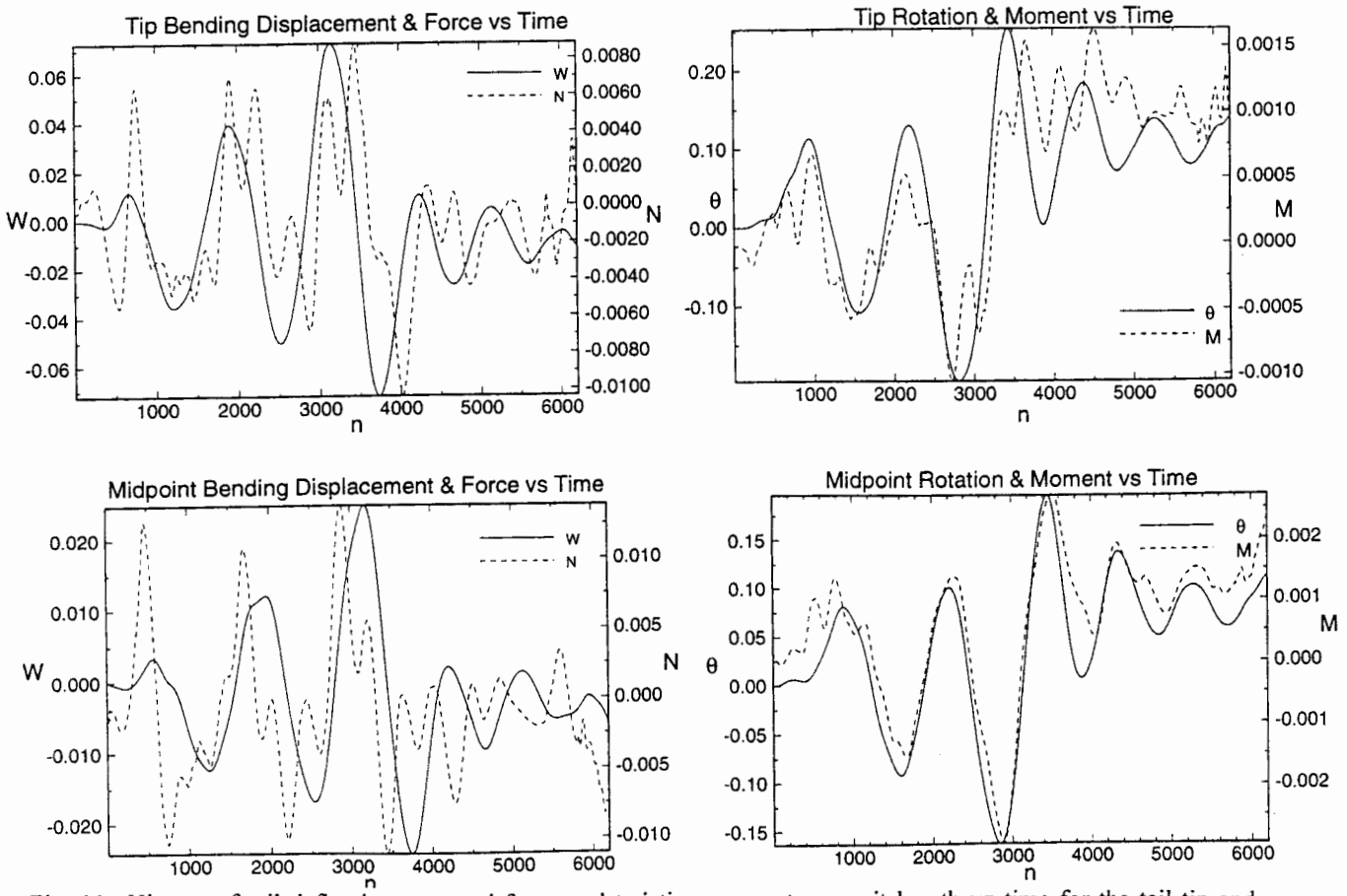

Fig. 11 History of tail deflections, normal-force and twisting-moment per unit length vz time for the tail tip and midpoint, it = 14,601–17,600 (uncoupled bending-torsion tail response).

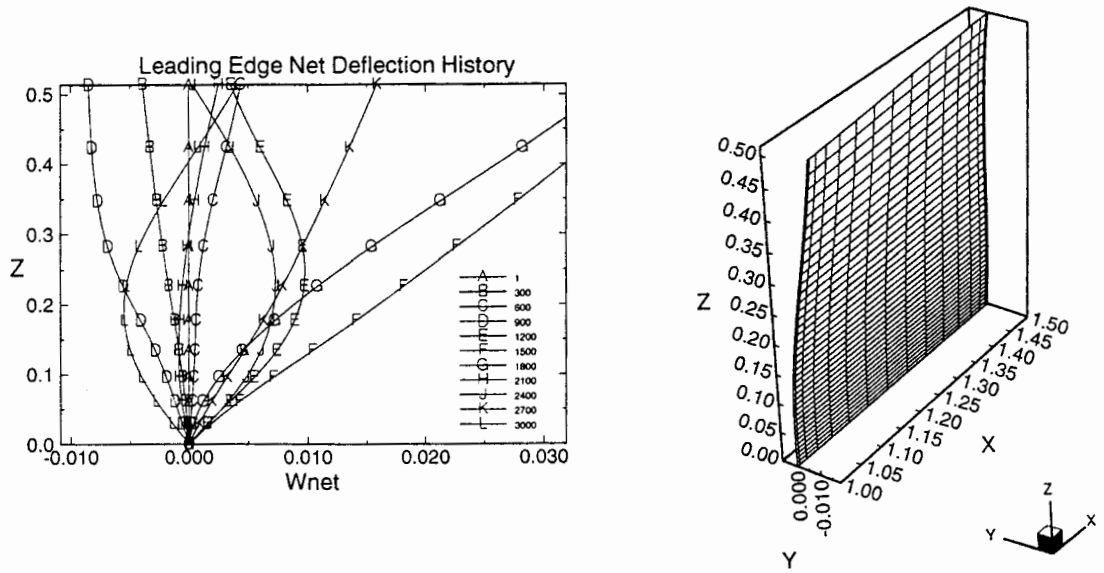

Fig. 12 History of tail total deflections over the tail and three-dimensional view of the tail at it = 21,600; it = 14,601–17,600 (coupled bending-torsion tail response).

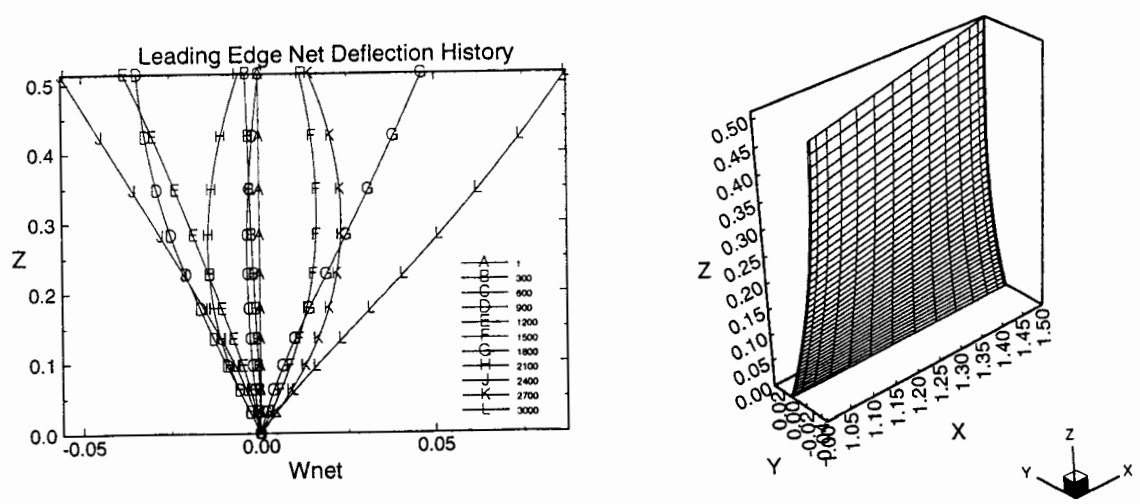

Fig. 13 History of tail total deflections over the tail and three-dimensional view of the tail at it = 21,000; it = 14,601–17,600 (uncoupled bending-torsion tail response).

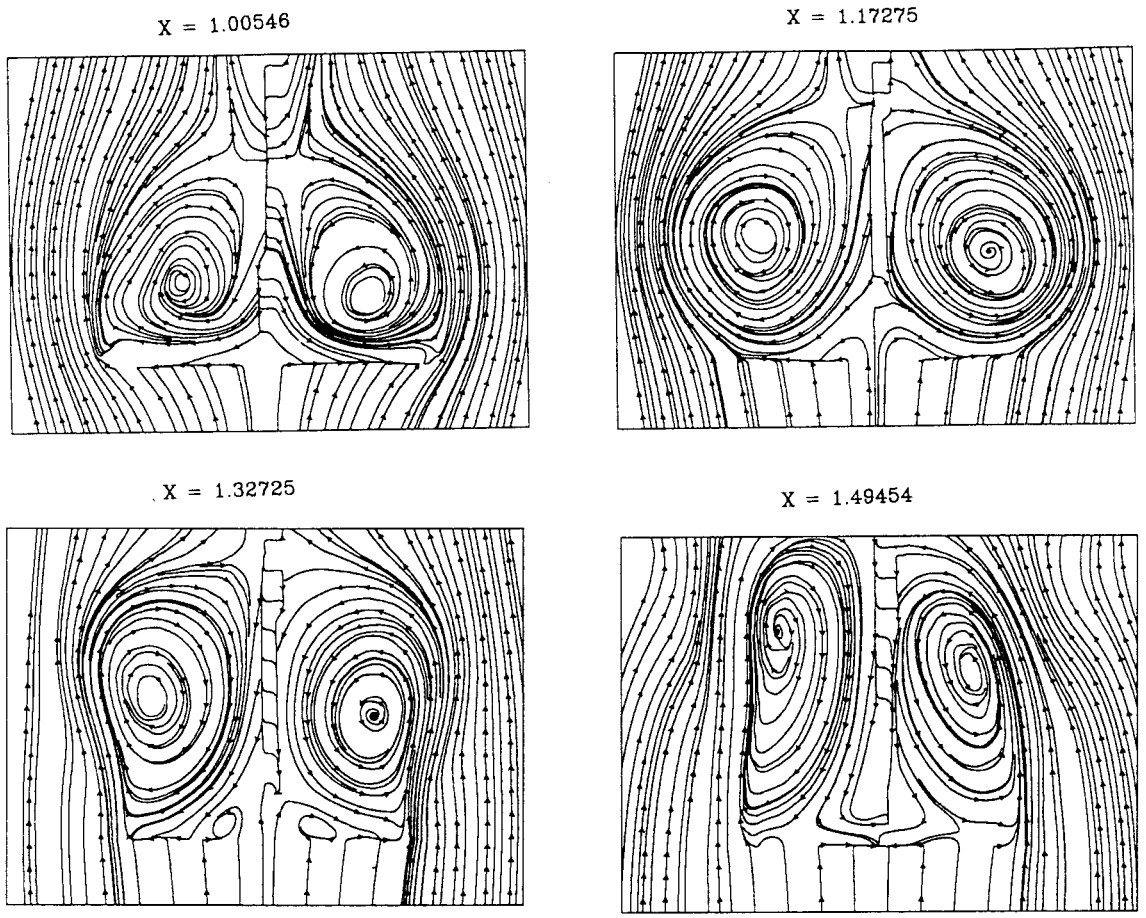

Fig. 14 Cross-flow instantaneous streamlines at different chord stations through the tail, it = 21,000 (coupled bending-torsion tail response).

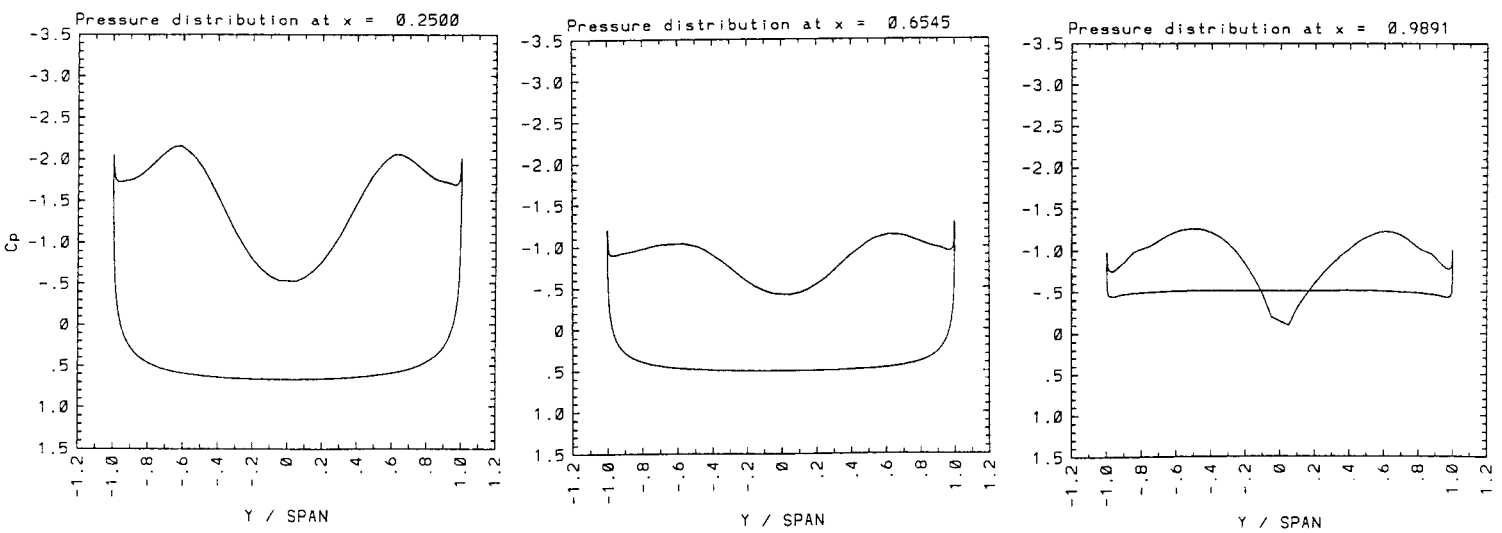

Fig. 15 Spanwise, surface-pressure coefficient at different chord stations on the wing; it = 16,600 (coupled bending-torsion tail response).